7.1 Introduction

In this chapter, an effort has been made to optimize the yttrium substitution in $SrAl_4Fe_8O_{19}$ hexaferrite. It is found from the literature that the substitution of RE^{+3} ions into hexaferrite lattice suppress the grain growth, lower the grain size and command the coercive force for large practical applications. The dielectric properties of the hexagonal ferrites mainly depend on the intrinsic electric dipole polarization and interfacial polarization. Substitution of RE^{+3} ions induce the difference of sizes in the system and form extra intrinsic electric moment. Thus, it is strengthen the dielectric properties. In addition, RE^{+3} ions also induce the lattice defects and effectively suppress the grain growth, which are also responsible for improving the resistivity of the system.

Jiang *et al*. (2016) have described that yttrium addition improves H_c in SrM. Niu and Zhang (2016) have stated that Y^{+3} ion helps to increase the remanence magnetization along with intrinsic coercivity in SrM. In addition, Ahmed *et al*. (2003) have reported that yttrium improves Curie temperature in NiZn ferrite. Therefore, substitution of this cation in $SrAl_4Fe_8O_{19}$ hexaferrite can produce novel material with modified properties.

In this work, yttrium substituted $SrAl_4Fe_8O_{19}$ ($SrAl_4Y_xFe_{8-x}O_{19}$ ferrites with x = 0.0, 0.05, 0.10, 0.20, & 0.30) ferrites have been synthesized by the auto combustion method, as discussed in section 3.1.1. To explore the structural parameters, Rietveld refinement is followed out. The effect of Y^{+3} substitution is investigated through density, microstructure, remanence (*Br*), coercivity, $(BH)_{max}$, Curie temperature, dielectric constant (ε) and resistivity measurement.

7.2 Results and Discussion

Figure 7.1 shows the FTIR spectra of dried calcined $SrAl_4Y_xFe_{8-x}O_{19}$ (x = 0.0, 0.05, 0.10, 0.20, & 0.30) ferrite powders. As reported earlier, hexaferrite has 189 optical modes and out of them only 31 (13 A_{2u} + 18 E_{1u}) are IR respond modes [Mahadevan *et al*. (2017)]. In this study, only three are active modes 443, 574 and 621 cm^{-1}. The absorption bands between 400 to 800 cm^{-1} are elucidated the characteristic bands of $SrFe_{12}O_{19}$ [Baykal *et al*. (2012b), Xie *et al*. (2012)]. In these bands, frequency around υ_1 (443) is attributed to the intrinsic elongation of the metal cation vibrations at the octahedral site & absorption frequencies around υ_2 (574, 621) are made due to the intrinsic elongation of the metal cation vibrations at the tetrahedral site [Auwal *et al*. (2016a), Mahadevan *et al*. (2017)].

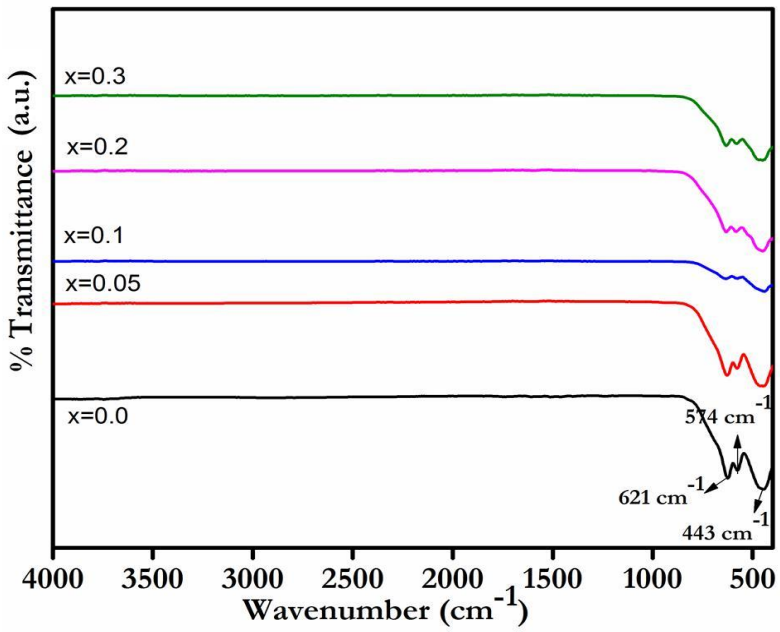

Figure 7.1 FTIR spectra of calcined $SrAl_4Y_xFe_{8-x}O_{19}$ ferrite samples.

From the graph, it is also found that band position is moved towards higher frequency and bands are broadened with substitutions. It indicates that Y^{+3} ions may occupy at the octahedral site [Gadkari *et al*. (2009)]. The shift towards higher frequencies may be due to

the decrease in bond length, which can be later linked to the reduction in lattice parameters, as shown in XRD. It can also be seen from the graph that the intensity of υ_1 band is decreased while, broadening is increased with substitution. It suggests that the system is more disorder [Bellad *et al*. (1998)]. The absence of the higher frequency band suggests the finishing of redox reaction for hexaferrite formation. From the Table 7.1, it is also found that the value of υ_1 and υ_2 is increased with Y^{+3} substitution. It may be due to perturbation taking place in Fe-O bands with Y^{+3} ions substitution [Gabal and Angari (2009)]. The similar results are anticipated with the earlier report by Pervaiz and Gul (2012) on RE (Gd, Nd, Eu) substituted cobalt ferrite.

Table 7.1 Wave numbers ($\upsilon_1$and υ_2) of calcined $SrAl_4Y_xFe_{8-x}O_{19}$ ferrite samples.

Composition	**Wave number υ_1 (cm^{-1})**	**Wave number υ_2 (cm^{-1})**	**Wave number υ_2 (cm^{-1})**
x = 0.0	443.61	574.76	621.05
x = 0.05	447.46	576.69	626.83
x = 0.10	448.75	577.69	630.55
x = 0.20	449.39	578.62	632.69
x = 0.30	450.19	582.47	633.69

Figure 7.2 (a) shows the XRD patterns of the sintered $SrAl_4Y_xFe_{8-x}O_{19}$ ferrite samples with yttrium content. XRD patterns have exhibited the characteristic peaks similar to the normal pattern of strontium hexaferrite with JCPDS # 720739 [Debnath *et al*. (2015)]. No other characteristic peaks of impurity are detected. This means that Y^{+3} and Al^{+3} ions go into the hexagonal structure properly with less troubling the host lattice of strontium ferrite. Auwal *et al*. (2016b) have also reported the single phase strontium hexaferrite with the

substitution of yttrium without any secondary phase. The structure of various compositions of $SrAl_4Y_xFe_{8-x}O_{19}$ ($0 \leq x \leq 0.3$) are also analyzed by Rietveld structure refinement using *P63/mmc* space group. The experimentally observed, Rietveld calculated and their difference of XRD patterns for $SrAl_4Fe_8O_{19}$ and $SrAl_4Y_{0.3}Fe_{7.7}O_{19}$ obtained by Rietveld refinement are shown in Figure 7.3. Rietveld refinement confirms that all peaks are related to the M-type hexagonal structure with *P63/mmc* space group. The Rietveld fitting for the compositions are also very good. The fitted patterns are in good matching with the experimental data indicating the better quality of the results. The refinement parameters are listed in Table 7.2.

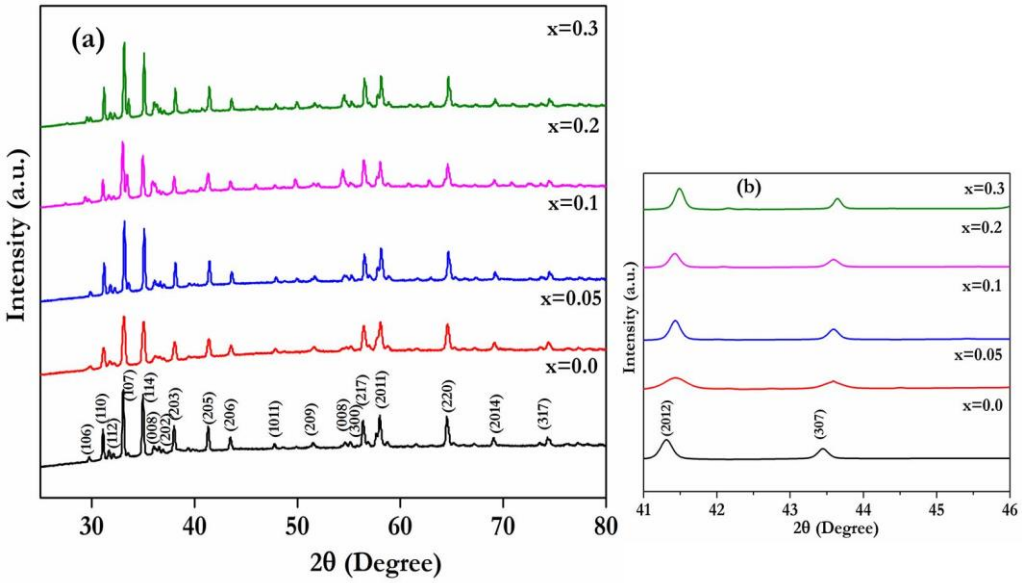

Figure 7.2 (a) XRD patterns of sintered $SrAl_4Y_xFe_{8-x}O_{19}$ samples, (b) XRD profiles shifting.

It is elucidated from the Table 7.2 that the values of '*a*' are nearly unaffected, whereas, '*c*' is slightly decreased with the increase in Y^{+3} content. Niu and Zhang (2014) have described that the lattice parameter is increased with the subsitution of larger radii element. But, in this study, the lattice parameter has been decreased, when Y^{+3} substitutes with Fe^{+3}. The substitution accounts for a strain in the lattice and appears local structural

disorder, which may limit the particle nucleation rate [Thakur *et al*. (2013b), Dunn (2016)]. Guner *et al*. (2016) have also reported the alike result with our observation.

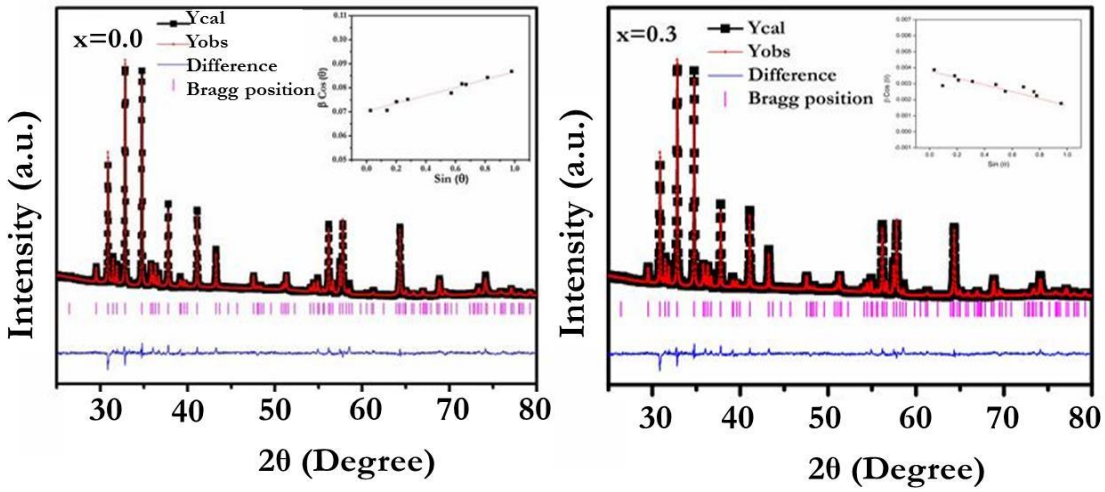

Figure 7.3 Rietveld refined XRD pattern of sintered $SrAl_4Y_xFe_{8-x}O_{19}$ samples with x = 0.0 and 0.3.

Table 7.2 Refinement parameters, Lattice parameter, volume, *c/a* ratio, strain, and crystallite size of sintered $SrAl_4Y_xFe_{8-x}O_{19}$ ferrite samples.

Composition	**R_p (%)**	**R_{wp} (%)**	**χ^2**	**Lattice parameter (Å)**		**Volume (Å^3)**	***c/a***	**Strain**	**Crystallite size (nm)**
				(a)	***(c)***				
x = 0.0	2.06	2.65	1.65	5.78	22.72	657.34	3.93	0.00413	12.64
x = 0.05	2.75	4.35	2.01	5.74	22.53	642.84	3.92	0.00478	47.46
x = 0.10	3.62	5.09	1.87	5.74	22.51	642.32	3.92	-0.000502	45.44
x = 0.20	3.95	5.62	2.21	5.74	22.47	641.24	3.91	-0.000537	36.47
x = 0.30	3.72	4.67	2.67	5.74	22.42	639.72	3.90	-0.000548	35.32

An important factor which validates the M-type structure is *c/a* ratio. In the present study, this ratio is <3.98, it confirms the magnetoplumbite structure formation [Rehman *et al*. (2017)]. From Figure 7.2 (b), it is also shown that the peak positions of the substituted samples are shifted to the higher angle compare to the pure ferrite sample. This increase in Bragg angle is attributed to the lattice strain and decreased in the lattice constant as well as cell volume (Table 7.2) of the system [Kumari *et al*. (2015)]. The diffraction pattern suggests some contraction is being induced in the system and results decrease in cell volume. The other reason can be understood by the occupation site. Y^{+3} ions may substitute Fe^{+3} in the octahedral site, but the ionic radius of the Y^{+3} ions is much bigger than the octahedral site. So, it may be understood that a small amount of Y^{+3} cations may substitute Fe^{+3} cations and may go into the octahedral sites by reorganizing of cations among the tetrahedral and octahedral site to lower the free energy. There may be a partial relocation of the ions between both the sites in order to slow down the strain at the octahedral sites. For this reason the lattice parameters decrease.

The calculations of the crystallite size and strain of all the sintered samples have been carried out by the broadening of the peaks using the Williamson–Hall (WH) approach, as discussed in equation 3.15. The WH plot for x = 0.0 and 0.3 of $SrAl_4Y_xFe_{8-x}O_{19}$ have been shown in inset Figure 7.3. From Table 7.2, crystallite size initially is increased at x = 0.05 substitution. Later, it is decreased with Y^{+3} substitution. Initial enhancement in crystallite size and micro strain can be understood by the mismatch of ionic radii. Ionic radii of Y^{+3} (0.93Å) substitutes Fe^{+3} (0.64Å) and it induces tensile strain in the system, as shown in Table 7.2 [Almessiere *et al*. (2019)]. Similar behavior is observed by the Liu *et al.* (2018). With further substitution, too much Y^{+3} content increases and it induces a compressive strain in the

structure. Conclusively, this too much Y^{+3} content is responsible for converting tensile strain to compressive strain up to x = 0.3 [Almessiere *et al*. (2019)]. For x = 0.3 sample shows a negative slope, which correlates a compressive strain in the lattice [Silva *et al*. (2015)]. The crystallite size is decreased with further Y^{+3} content. This may be explained on the basis of Y^{+3}, which suppresses the crystal grain's growth. The decrease in crystallite size probably reduces the crystal axis ratio thereby increasing compressive strain in the system [Meng *et al*. (2009)].

Table 7.3 Grain size and elemental composition of sintered $SrAl_4Y_xFe_{8-x}O_{19}$ ferrite samples.

Composition	Grain size (μm)	Elemental composition (At%)			
		Sr	Al	Y	Fe
x=0.0	1.11	3.07	14.09	-	34.31
x=0.05	1.16	2.83	13.79	0.14	28.36
x=0.10	0.72	3.17	13.50	0.64	25.43
x=0.20	0.71	2.96	13.82	0.65	21.79
x=0.30	0.70	3.05	14.06	1.83	20.74

Table 7.3 shows the grain size of the Y^{+3} substituted ferrites along with elemental analysis. Microstructure of the specimen is shown in Figure 7.4. SEM image reveals that the grains become more rounded on the edges, more irregular shaped, and less clearly hexagonal with increasing Y^{+3} content. The grain size initially is increased at x = 0.05 further, it is decreased with Y^{+3} content. This initial increment can be understood by the mismatch of ionic radii [Almessiere *et al*. (2019)]. Larger ionic radii Y^{+3} (0.93 Å) is substituted with the smaller ionic radii ion Fe^{+3} (0.64 Å). This leads to induce the tensile strain in the system [Almessiere *et al*. (2019)]. With further Y^{+3} substitution in the system, it becomes

responsible for generating the lattice compressive strains and internal stress [Zhong *et al*. (2018)] in the lattice. Such stress can obstruct the growth of the grains. Another reason for decreasing the grain size may be due to that excess amount of Y^{+3}, which may not encourage the growth of the grains in strontium hexaferrite [Irfan *et al*. (2016)].

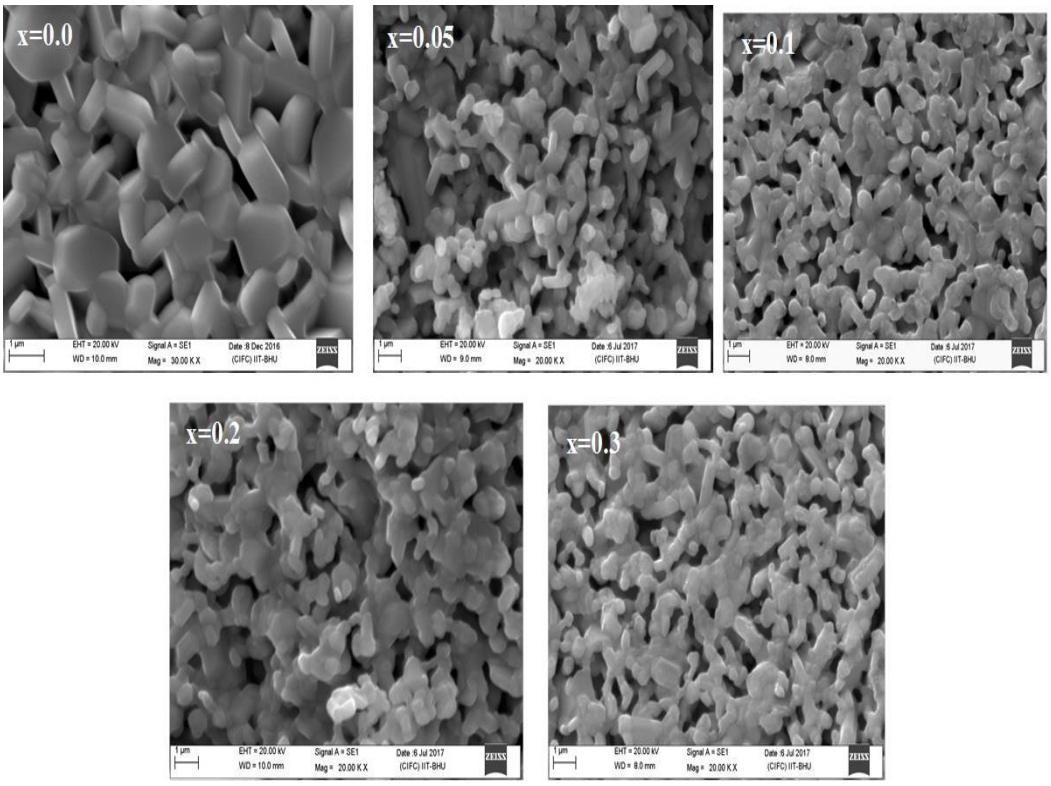

Figure 7.4 SEM micrographs of sintered $SrAl_4Y_xFe_{8-x}O_{19}$ ferrites.

EDX elemental analysis is performed to confirm the chemical composition of sintered $SrAl_4Y_xFe_{8-x}O_{19}$ ferrites, as presented in Figure 7.5. Table 7.3 presents the At % of Sr, Al, Y, and Fe in sintered hexaferrites. It shows that At% of Y^{+3} is increased while, Fe^{+3} is decreased with increasing 'x'. The elemental mapping micrographs of $SrAl_4Y_xFe_{8-x}O_{19}$ of x = 0.0 and 0.3 are shown in Figure 7.6. It is showed that Sr, Al, Y, Fe, and O are dispersed homogeneously in all over the sample and gives the confirmation of purity of samples.

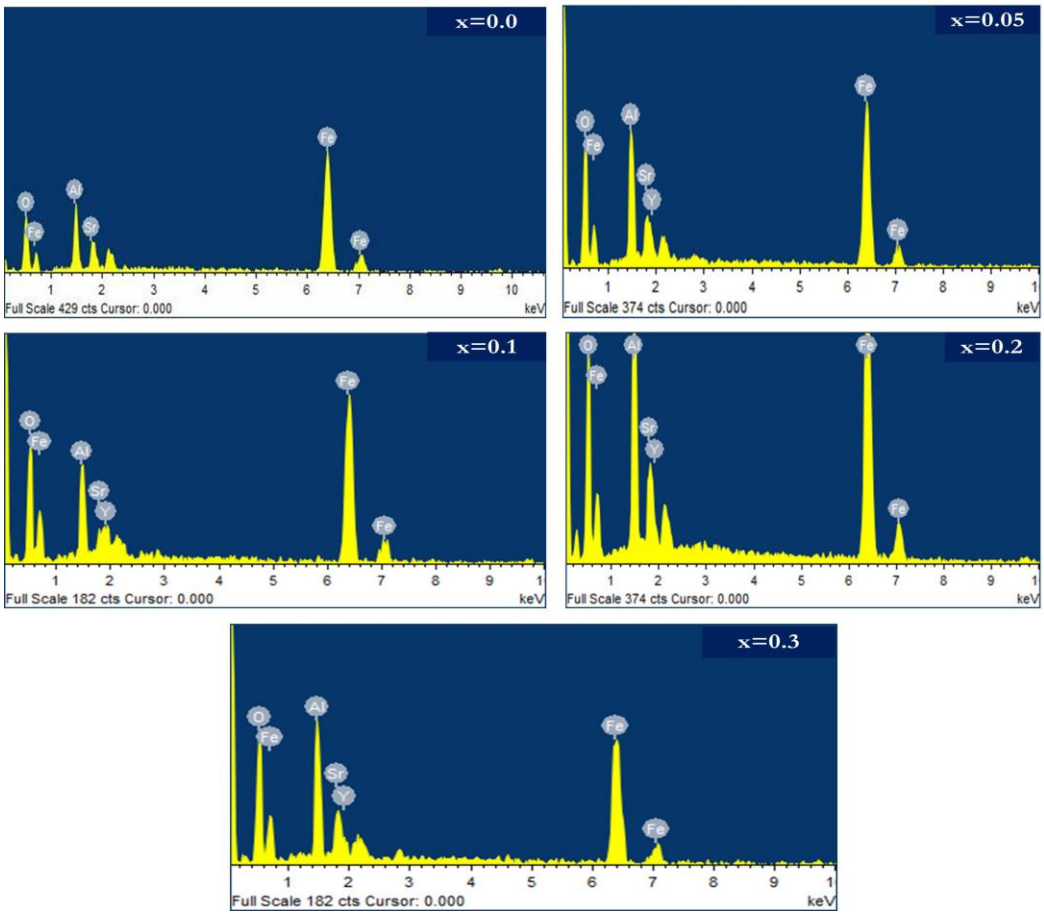

Figure 7.5 EDX micrograph of sintered $SrAl_4Fe_{8-x}Y_xO_{19}$ ferrites.

Figure 7.7 to Figure 7.11 shows the magnetic behavior of Y^{+3} substituted, i.e., $SrAl_4Y_xFe_{8-x}O_{19}$ (x = 0.0, 0.05, 0.1, 0.2, & 0.3) hexaferrites at room temperature. Figure 7.7 demonstrates the *M–H* loops of $SrAl_4Y_xFe_{8-x}O_{19}$ ($0 \leq x \leq 0.3$) hexaferrites. From the figure, it is found that M_s continuously decreases and H_c increases with the substitution. Figure 7.8 shows the variation of ramenence (*Br*) and bulk density with the function of Y^{+3} content. With substitution, it is also found that the bulk density is improved. The improvement may be due to the higher atomic weight yttrium (88.90 amu) replaces the lower atomic weight iron (55.84 amu) in the structure [Ishaque *et al.* (2010)].

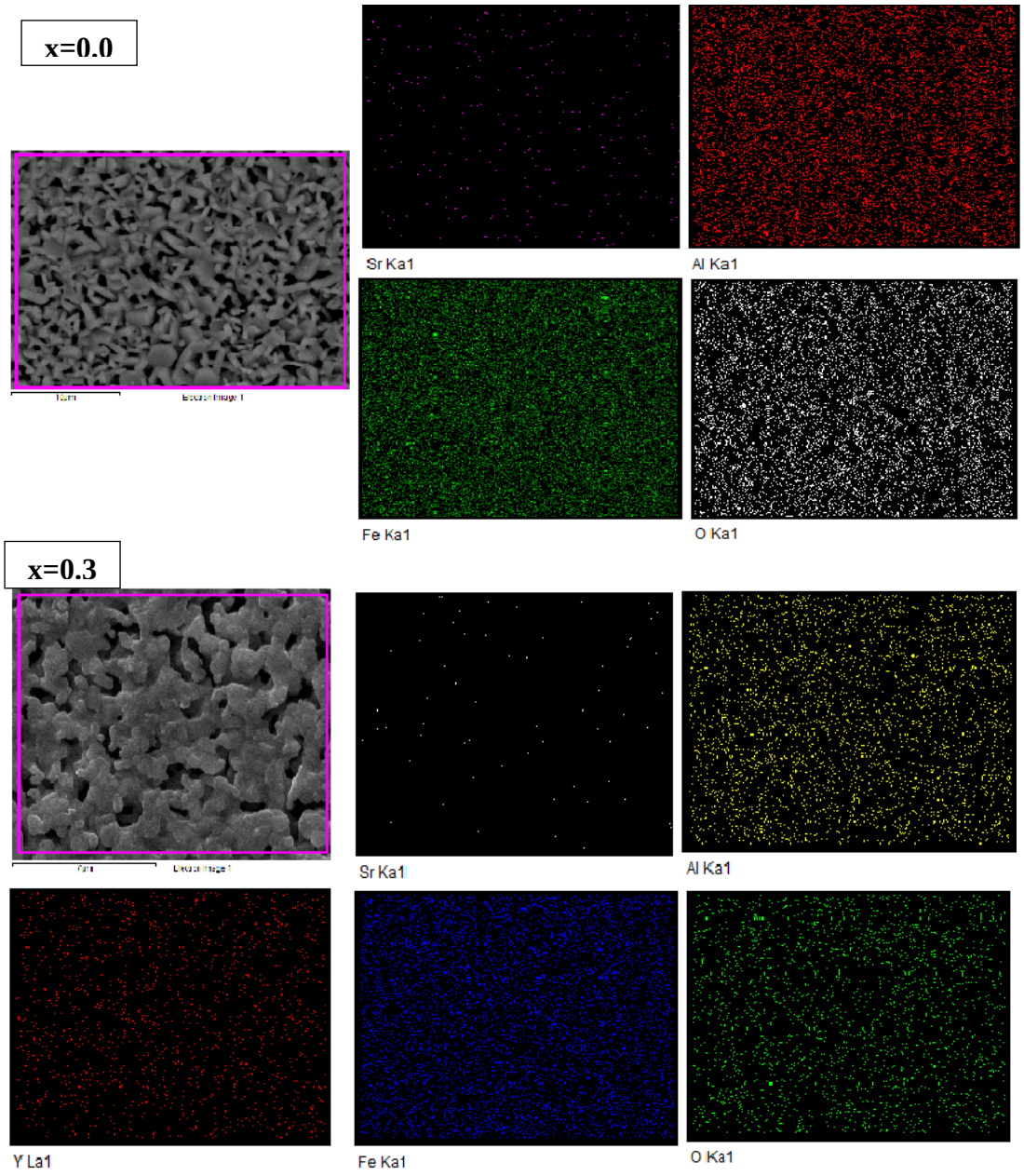

Figure 7.6 Elemental mapping micrographs of $SrAl_4Y_xFe_{8-x}O_{19}$ (where, x = 0.0 and 0.3).

The second reason may be due to the restraining of grain growth with Y^{+3} content during sintering [Irfan *et al.* (2014)]. Suharno *et al.* (2014) have also reported that Y^{+3} helps in the densification in the ceramics. The values of ramenence (*Br*), Bohr magnetons (μ_B),

coercivity and squareness ratio have been shown in Table 7.4 along with anisotropy constant (k_{eff}), $(BH)_{max}$, and Tc (°C).

Table 7.4 *Br*, μ_B, iH_c, bH_c, H_k/iH_c, k_{eff}, $(BH)_{max}$ and Tc of sintered $SrAl_4Y_xFe_{8-x}O_{19}$ ferrite samples.

Composition	***Br*** **(kG)**	μ_B	iH_c **(kOe)**	bH_c **(kOe)**	H_k/iH_c	$k_{eff\ x10}^{6}$ **(erg/cm^3)**	$(BH)_{max}$ **(MGOe)**	**Tc (°C)**
x=0.0	4.10	4.02	18.15	18.02	0.89	3.54	6.03	320
x=0.05	4.01	1.59	26.46	25.00	0.91	3.77	5.71	472
x=0.10	3.35	1.24	30.00	29.00	0.93	3.94	4.25	513
x=0.20	2.11	0.75	36.00	35.50	0.88	4.15	3.63	614
x=0.30	3.02	1.07	33.00	32.00	0.90	3.92	4.48	325

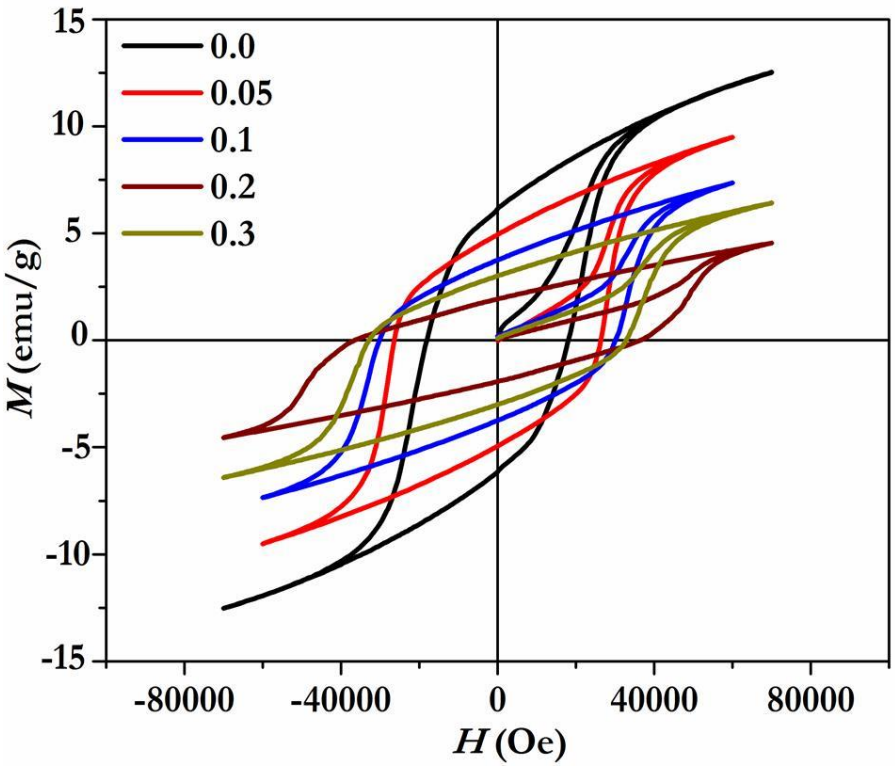

Figure 7.7 *M-H* curves of $SrAl_4Y_xFe_{8-x}O_{19}$ ($0.0 \leq x \leq 0.3$) hexaferrites.

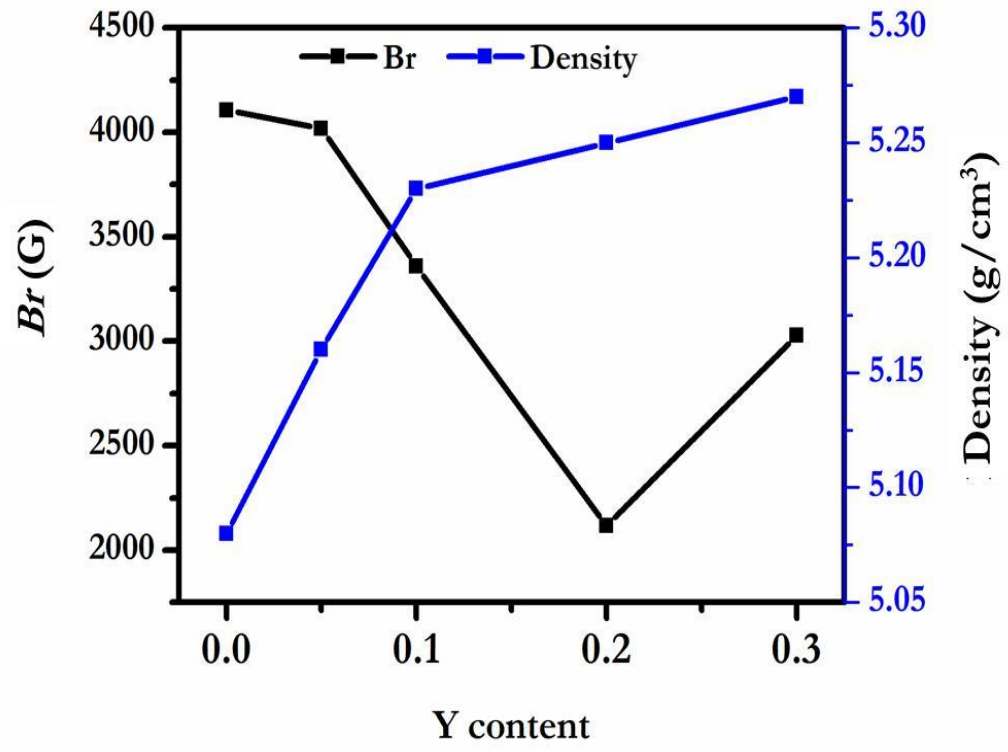

Figure 7.8 Variation of *Br* with density as a function of Y^{+3} content.

Br is decreased with Y^{+3} substitutions up to x = 0.20. It can be described by the intrinsic magnetic properties, which mainly depend on site occupation of cation, ionic radii, etc. The smaller ionic radii ion Fe^{+3} is being replaced by larger ionic radius Y^{+3}. It produces the local strain, which may cause the disorder and adjustment of local electronic states [Moon *et al*. (2019)]. In the hexagonal structure, Fe^{+3} present in five different sites, like three octahedral sites (*2a*, *12k*, & $4f_2$), one trigonal bipyramidal site (*2b*) & one tetrahedral site ($4f_1$). At *2a*, *12k* and *2b* sites, Fe^{+3} ions are arranged in spin up position and at $4f_1$ and $4f_2$ sites, Fe^{+3} ions are arranged in spin-down position [Rehman *et al*. (2017)]. In present case, Y^{+3} substitutes Fe and it may go to any of five sites of Fe. But from the Table 7.4, it is found that *Br* decreases up to x = 0.2 due to the substitution of nonmagnetic Y^{+3} ion (Y^{+3} = $0\mu_B$) [Irfan *et al*. (2016)], which decreases the overall magnetic moment as we can see the value of

magnetic moment from the Table 7.4. The Bohr magnetron shows that it is decreased with Y^{+3} content. This decrease can only be explained by considering that Y^{+3} nonmagnetic cations ($\mu = 0\mu_B$) replace magnetic Fe^{+3} cations ($\mu = 5\mu_B$) in the octahedral sublattice. The decrease in μ_B with yttrium agrees with the decrease in *Br*. It may also consider that the RE substitutions are weakened the super-exchange interactions between one oxygen atom (Fe^{+3}–O–Fe^{+3}) and two oxygen atoms (Fe^{+3}–O–O–Fe^{+3}) because of its strongly distorted environment, which leads to the drastic decrease of the *Br* value for the samples [Thongmee *et al*. (2003), Jiang *et al*. (2016)]. Overall, magnetic Fe^{+3} is being substituted by the non-magnetic Y^{+3}, causes the decrease of the total magnetic moment [Ahmed *et al*. (2003), Jiang *et al*. (2016)] in the matrix. Thongmee *et al*. (2003) have reported that larger ions have a higher probability to go in the octahedral site, whereas smaller ions may go to the tetrahedral site. Y^{+3} ions are bigger than the Fe^{+3} ions so, Y^{+3} may be substituted at the octahedral site. Auwal *et al*. (2016b) also have reported the same. From the Table 7.5, it is found that bond length of octahedral site continuously decreases up to x = 0.20, this indicates that Y^{+3} may be substituted at octahedral sites. Meanwhile, the bond length of tetrahedral site is also decreasing with the substitution, this happens because of the Fe^{+3} ions, which relocate towards the tetrahedral site [Auwal *et al*. (2016b)]. *Br* is increased with further increased the nonmagnetic cations at x = 0.30. Auwal *et al*. (2016b) have reported that further increasing of nonmagnetic ions, substitution has been started at the tetrahedral site instead of the octahedral site. The same observation is reported by Chakrabarty *et al*. (2018). From the Table 7.5, the bond length of octahedral remains constant at x = 0.30, but for the tetrahedral site bond length keeps decreasing. This is also indicating that substitution is being taken place at the tetrahedral site. At tetrahedral position $4f_1$ site Fe^{+3} ion present in the spin-down

position, so nonmagnetic ions substitute the spin down cations and increase the overall magnetic moment (μ_B) of the system, as we can see from the Table 7.4 that magnetic moment is also increased at x = 0.30. The other reason to increase *Br* may be due to the suppression of the spin cycloid [Chaktaborty *et al*. (2013)].

Table 7.5 Average Fe-O bond lengths in $SrAl_4(Cr_{0.5}Sn_{0.5})_xFe_{8-x}O_{19}$ with ($0 \leq x \leq 0.8$).

Site	Bond Type	0.0 Avg.	0.05 Avg.	0.1 Avg.	0.2 Avg.	0.3 Avg.
Fe1 (*2a*, O)	Fe-O	1.931	1.929	1.923	1.905	1.904
Fe2 (*2b*,TBP)	Fe-O	1.793	1.790	1.791	1.790	1.793
Fe3 ($4f_1$,T)	Fe-O	2.031	1.986	1.881	1.847	1.819
Fe4 ($4f_2$,O)	Fe-O	2.086	1.987	1.945	1.908	1.907
Fe5 (*12k*,O)	Fe-O	1.976	1.964	1.941	1.912	1.912

The variation in iH_c with Y^{+3} content is indicated that the iH_c is improved with Y^{+3} content upto x = 0.20, as shown in Figure 7.9. It is well recognized that this behavior depends on the magneto-crystalline anisotropy constant (k_{eff}) and grain size [Almessiere *et al*. (2018)]. Table 7.4 shows that k_{eff} continuously is increased with Y^{+3} substitution. Grain sizes are also decreasing with Y^{+3} content. Decreasing in grain size is responsible for increasing the grain boundaries that contribute into the obstruction of domain wall motion. Smaller the grain sizes, larger will be the grain boundaries which perform as pinning sites for the domain wall movement and it leads to restrict the rotation of magnetization [Thakur *et al*. (2013b)]. So, the coercivity is increased with the reduction in grain size. The decrease in H_c for x = 0.30 composition may be because of a decrease in anisotropy constant.

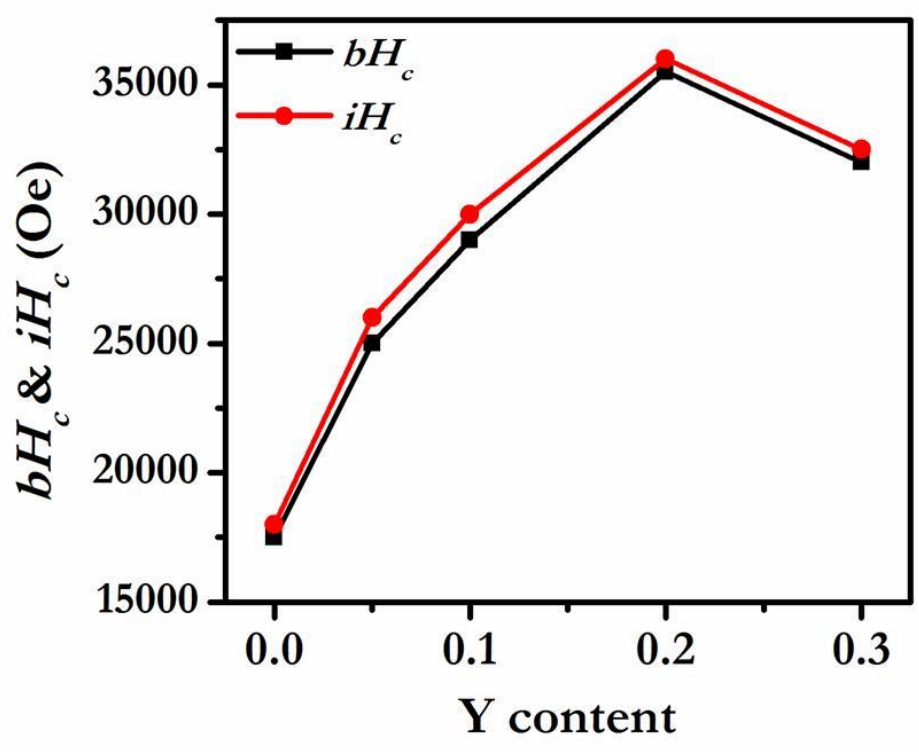

Figure 7.9 Variation of bH_c & iH_c as a function of Y^{+3} content.

This variation of grain size with coercivity can also be analyzed on the basis of the crystal anisotropy [Singhal *et al*. (2010)]. Magnetic anisotropy is estimated from the law of approach, as discussed in described in section 3.4.4 and Figure 7.10 shows the typical *M* versus $1/H^2$ curve for $SrAl_4Y_xFe_{8-x}O_{19}$ for x = 0.0 and x = 0.3. Table 7.4 shows the variation of k_{eff} value as a function of Y^{+3}. k_{eff} is increased with Y^{+3} content up to x = 0.20, resultant coercivity increases with Y^{+3} content. The decrease in k_{eff} for x = 0.30 may be because of increase in Br or decrease in spin-orbit coupling [Kumari *et al*. (2015)]. The anisotropy also depends on the super-exchange coupling [Nlebedim *et al*. (2009)]. The non-magnetic Y^{+3} cation may not get into in super-exchange interaction. So, there is a decrease in the super-exchange coupling that decreases the anisotropy.

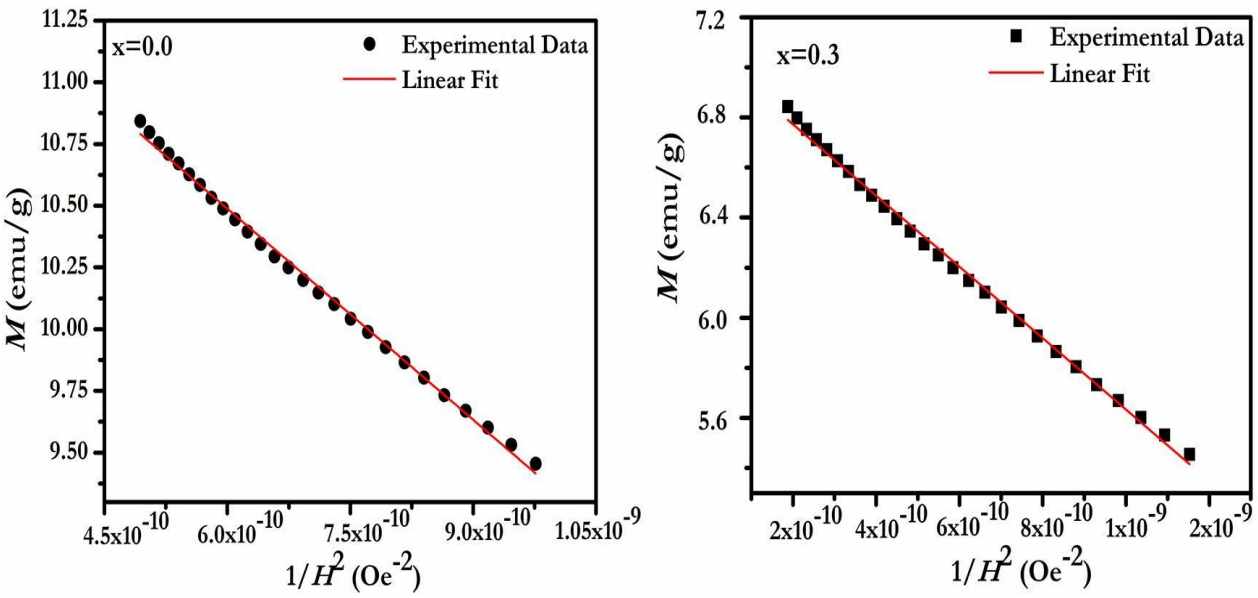

Figure 7.10 Variation of M vs $1/H^2$ for x = 0.0 and 0.3 Y^{+3} composition.

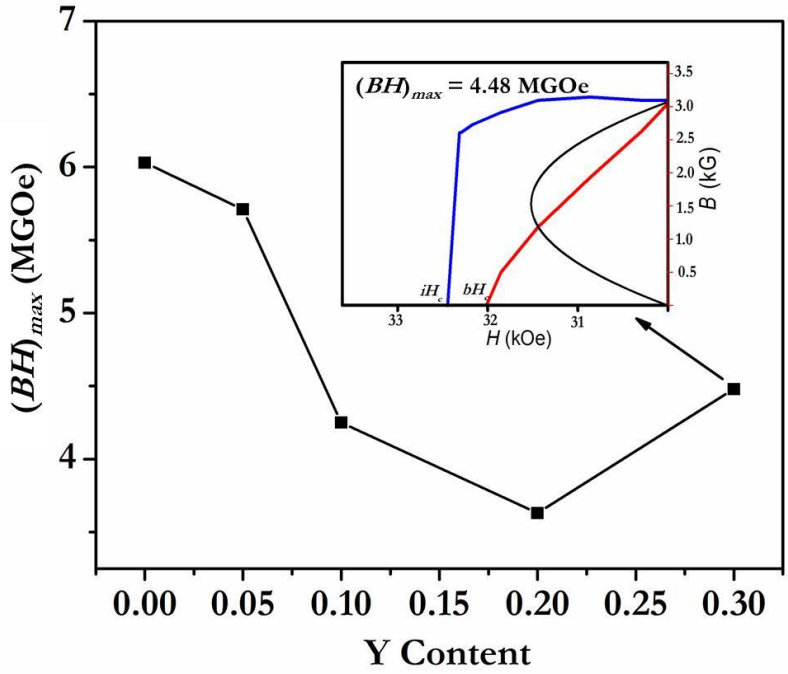

Figure 7.11 Variation of $(BH)_{max}$ as a function of Y^{+3} content.

Table 7.4 shows the variation of the squarness ratio (H_k/iH_c) with Y^{+3} content. Table 7.4 shows this ratio is >0.85, which belongs to permanent magnet. Figure 7.11 shows the

energy $(BH)_{max}$ with the function of Y^{+3} content. It is decreased with the substitution up to x = 0.2. The demagnetization curve of x = 0.3 is shown in inset Figure 7.11.

Table 7.4 shows the behavior of Curie temperature with Y^{+3} content. Curie temperature demonstrates a divergence due to a phase transition of second order. For $SrAl_4Y_xFe_{8-x}O_{19}$ samples, the ferrimagnetic–paramagnetic phase transition is usually a phase transition of second-order [Trukhanov *et al*. (2017b)]. An increase in Y^{+3} concentration, the temperature of the phase transition smoothly increases from 320 °C for x = 0.0 to 614 °C for x = 0.20 composition. It is higher than for the pure strontium hexaferrite [Ahmed *et al*. (2003)]. Increase in Curie temperature may be because of the increase in magnetic anisotropy with Y^{+3} content in the system [Rai *et al*. (2013b)]. Ahmed *et al*. (2003) also have reported that Y^{+3} helps to increases the Curie temperature. Further increased in Y^{+3} at x = 0.30, Tc is decreased. The decrement of Tc may be due to a decrease in the B-site interaction where, Y–Y and Y–Fe interaction are lesser liken to Fe–Fe interactions, as Fe–Fe interactions are dominant one [Gadkari *et al*. (2013)]. The other reason may be because of the spin canting structure which is induced and produced the deviation from the collinear to a non-collinear arrangement [Liu *et al*. (2002b)].

Figure 7.12 expresses the dielectric behavior of the sample with respect to the frequency from 20 Hz to 20 MHz. The dielectric parameter of strontium hexaferrite is affected by many physical parameters, such as synthesis techniques, sintering conditions, chemical composition, particle sizes, etc [Ashiq *et al*. (2012)]. It is observed from the curve that dielectric constant reduces with frequency. The variation of dielectric properties with frequency mainly contingent on the of interfacial and intrinsic electric dipole polarization [Sadiq *et al*. (2015)]. According to Koop's phenomenological theory, polarization in ferrite is

due to the limited displacement of an electron between $Fe^{+2} \leftrightarrow Fe^{+3}$ with an applied field [Singh *et al*. (2010)]. The compositional effect at 1 MHz frequency on the dielectric constant is shown in Table 7.6. It is decreased with Y^{+3} content. The decrement may be explained by the deficiency of iron ions in the occupied site. Irfan *et al.* (2016) have reported that Y^{+3} has the preference to reside in the octahedral site. Iron ions are being substituted by Y^{+3} ions at the octahedral site, so the numbers of iron ions are decreased in the system. Resultant, hopping of electrons is decreased among ferric and ferrous ions at the octahedral site and obstructs the displacement of space charge carriers with the electric field [Ashiq *et al*. (2012)]. Therefore, the dielectric constant is decreased. The synthesized samples have much lower dielectric constant (20.28 at 1 MHz) than the bulk synthesized sample (959.3 at 1 MHz) [Shakoor *et al*. (2014)].

Table 7.6 Dielectric constant and resistivity of sintered $SrAl_4Y_xFe_{8-x}O_{19}$ ferrite samples at 1 MHz.

Composition	**Dielectric constant (Ɛ) at 1MHz**	**ρ (Ω-cm) x 10^4 at 1MHz**
0	20.52	5.54
0.05	20.32	8.30
0.1	20.29	9.20
0.2	20.28	11.60
0.3	19.62	13.80

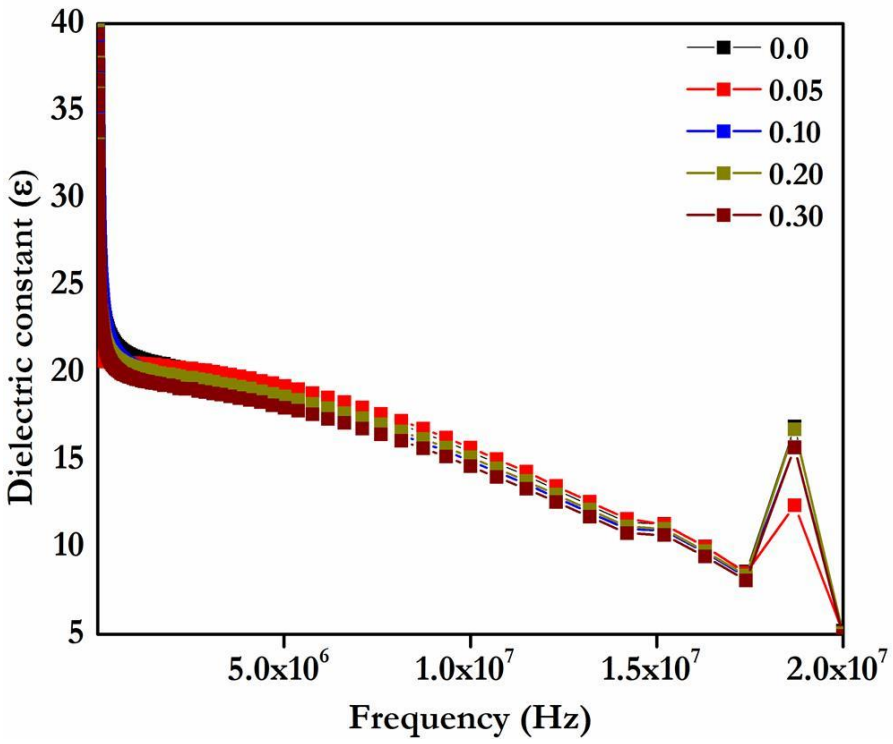

Figure 7.12 Plot of dielectric constant (ε) versus frequency for $SrAl_4Y_xFe_{8-x}O_{19}$ ferrites.

Figure 7.13 shows the changes of resistivity with frequency. All samples are demonstrated the common behavior, where resistivity (ρ) reduces with increase in the frequency. It is clear that high resistivity is observed at a lower frequency. It can be interpreted by the conduction mechanism. It induces on the base of hopping of charge carriers among the Fe^{+2} and Fe^{+3} ions on octahedral site. As the frequency is increased, external field increases the hoping of charge carriers ensuing in an improvement in the conduction process and decreases the resistivity. It has been also found that the resistivity is increased with Y^{+3} content. This behavior of resistivity with the composition can be explained by grain sizes. Ishaque *et al*. (2016) have reported that small grain sizes cause high

resistivity because they have a large area of grain boundary. These grain boundaries act as dispersion center for the flowing of electrons and hence grain boundaries are highly resistive.

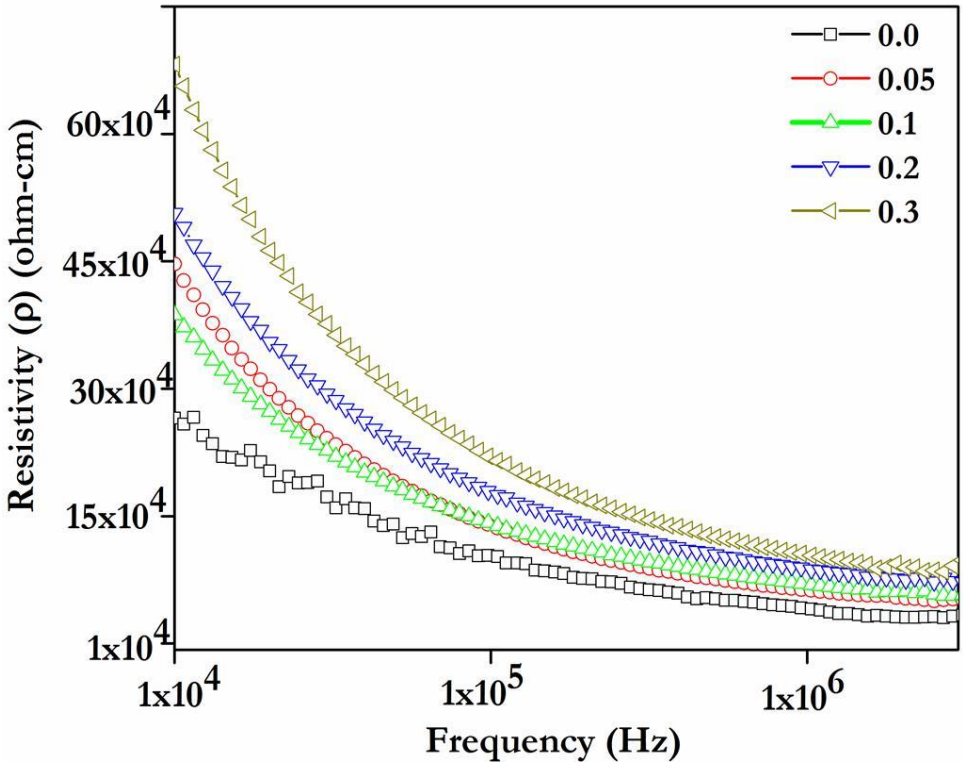

Figure 7.13 Resistivity versus frequency of $SrAl_4Y_xFe_{8-x}O_{19}$ ferrites.

7.3 Summary

Y^{+3} ion substituted $SrAl_4Y_xFe_{8-x}O_{19}$ ferrite nanoparticles are synthesized successfully by the auto combustion method. The XRD study reveals the phase formation of M-type hexaferrite with no secondary phases. The grain size of the matrix decreases with increase in Y^{+3} ions. In magnetic properties, it is found that the coercivity is enhanced from 18 kOe to 36 kOe by Y^{+3} inclusion due to decrease in grain size. Dielectric spectra and resistivity both are decreasing with respect to frequency. With Y^{+3} substitution, the resistivity increases from $5.43x10^4$ - $13.80x10^4$ Ω-cm. The Curie temperature & anisotropy field increase with Y^{+3} substitutions.